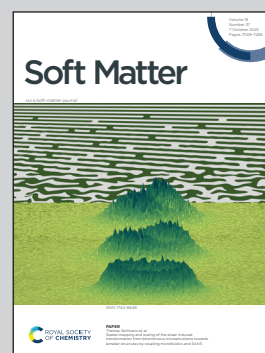


Showcasing research performed in collaboration between the University of Manchester and the University of Luxembourg.

Curvature-mediated programming of liquid crystal microflows

Leveraging liquid crystals in complex microfluidic systems offers unique avenues for flow control.

As featured in:



See Kamil Fedorowicz,  
Anupam Sengupta *et al.*,  
*Soft Matter*, 2023, **19**, 7084.



Cite this: *Soft Matter*, 2023,  
19, 7084

# Curvature-mediated programming of liquid crystal microflows

Kamil Fedorowicz,<sup>ib</sup>\*<sup>a</sup> Robert Prosser<sup>a</sup> and Anupam Sengupta<sup>ib</sup>\*<sup>b</sup>

Despite the recognized role of liquid crystal microfluidics in generating programmable, self-organized and guided flow properties, to date, the flow behavior of LCs within curved channels remains unexplored. Using experiments and numerical simulations, we demonstrate that the curvature of microscale conduits allow programming of liquid crystal (LC) flows. Focusing on a nematic LC flowing through U- and L-shaped channels – two simple yet fundamental curved flow paths – with rectangular cross-section, our results reveal that the curvature of flow path can trigger transverse flow-induced director gradients. The emergent director field feeds back into the flow field, ultimately leading to LC flows controlled by the channel curvature. This curvature-mediated flow control, identified by polarizing optical microscopy and supported by the nematofluidic solutions, offers concepts in LC microfluidic valves, wherein the throughput distribution is determined by the Ericksen number and variations in local curvature. Finally, this work leverages curvature to amplify (suppress) LC transport through flow-aligned (homeotropic) regions emerging within channels with bends, in a programmable manner. Our results demonstrating the dependence of the dynamic flow-director coupling on the local curvature will have far-reaching ramifications in advancing the understanding of LC-based passive and active biological systems under real life geometrical constraints.

Received 28th June 2023,  
Accepted 29th August 2023

DOI: 10.1039/d3sm00846k

[rsc.li/soft-matter-journal](http://rsc.li/soft-matter-journal)

## 1. Introduction

Microfluidics, the science and technology of flow manipulation at microscale,<sup>1,2</sup> touches every sphere of our lives today.<sup>3–5</sup> Microfluidic devices combine several laboratory processes into a single low-footprint instrument; their compactness, reduced analysis cost and lower testing times make them a potential competitor for current large-footprint devices.<sup>6–9</sup> Although traditionally, microfluidics has been based on isotropic fluids, either Newtonian or complex fluids, recent advances in the field of liquid crystal microfluidics<sup>10</sup> have demonstrated unique potential of LCs in creating tunable fluid flows and fluidic properties at microscale.<sup>11–14</sup>

Nematic liquid crystals (NLCs), mesogens comprising rod- or disc-like molecules,<sup>15</sup> combine liquid fluidity with crystalline properties, thus offering distinct attributes which arise due to the coupling between the molecular alignment (referred to as the director field  $\mathbf{n}$ <sup>16</sup>), hydrodynamics and confinement effects.<sup>10,17</sup> LCs form systems with a non-zero orientational order, and the resultant material properties (hydrodynamic,

optical, electrical *etc.*) depend on the mean local director alignment. Controlling the emergent flow behavior *via* the interplay of elastic, viscous, and surface forces enable unique dynamical properties, offering mechanisms to manipulate LC flows.<sup>18–20</sup> Together with geometry of the flow conduits, and the anchoring conditions on the confining surfaces, the bulk director field and the resulting NLC flows fields are established.<sup>21–23</sup> The anisotropic viscosity of NLCs has already been exploited in non-intrusive flow control devices,<sup>22,24</sup> where the effective viscosity of each channel within a complex microfluidic network is governed by the interplay of surface anchoring and flow speed. Much of potential applications of liquid crystals arise from their anisotropic birefringence: the sensitivity of nematics to external field is essential in tunable lenses,<sup>25</sup> color filters,<sup>26</sup> optical<sup>27,28</sup> and biochemical<sup>29</sup> sensors. Furthermore, improving the responsiveness of NLCs to external fields provides pathways to manufacture novel microdisplay and information processing devices.<sup>26,30,31</sup> The behavior of the NLC flows in rectangular channels<sup>11,32</sup> emerges due to the competition between elastic and viscous effects, captured by the dimensionless Ericksen number,  $Er$ ;<sup>16</sup> microstructure ordering is governed by elastic (viscous) effects in  $Er \ll 1$  ( $Er \gg 1$ ) flows.

Historically, NLC studies were motivated by the development of liquid display devices, where flat channels (width  $\gg$  height) simplified the problem to two dimensions,<sup>33–39</sup> however with limited relevance to real microfluidic settings, where the

<sup>a</sup> School of Engineering, The University of Manchester, Manchester M13 9PL, UK.  
E-mail: [kamil.fedorowicz@manchester.ac.uk](mailto:kamil.fedorowicz@manchester.ac.uk)

<sup>b</sup> Physics of Living Matter Group, Department of Physics and Materials Science, University of Luxembourg, 162 A, Avenue de la Faïencerie, L-1511 Luxembourg City, Luxembourg. E-mail: [anupam.sengupta@uni.lu](mailto:anupam.sengupta@uni.lu)



channel height and width are comparable.<sup>11,40,41</sup> While these recent efforts have successfully attained tunable LC flows by combining appropriate surface anchoring, confinements, and hydrodynamic forcing, the role of channel curvature has been explored in little detail. Interestingly, curved geometries have been known to impact the behavior of both thermotropic and lyotropic LC systems,<sup>42</sup> including the spontaneous emergence of chiral structures from an otherwise achiral phase, for instance in lyotropic chromonic liquid crystals.<sup>43,44</sup> Confining the latter material into spherical structures is expected to be a promising avenue for novel flow control methods.<sup>45</sup> However, the flow behavior of chromonic phases in curved microfluidic channels, as well, remains to be investigated. In comparison, flows of isotropic fluids through curvilinear microchannels have received extensive attention for many decades, with distinct curvature-induced fluid dynamic outcomes.<sup>46–49</sup> In the case of Newtonian fluids, secondary flows in curved pipes are driven by the combination of fluid inertia and geometry curvature.<sup>46,49</sup> The secondary flow is strengthened when the fluid is viscoelastic because the positive first normal stress difference, arising from microstructure deformation, has an additive effect with inertia.<sup>49,50</sup> Our current understanding of LC flows through complex microfluidic geometries is limited to a few studies, such as those conducted within rectangular channels with obstacles<sup>51</sup> and at topological flow junctions.<sup>52,53</sup> Initial insight into the physics of microstructure ordering and its effect on the secondary flow in curved geometries was provided by Fedorowicz and Prosser,<sup>54,55</sup> who numerically investigated LC flows in capillary bends using the Leslie–Ericksen theory. Their results demonstrate that, similar to viscoelastic fluids, the secondary flow is driven by the interaction of normal stresses with flow curvature. In the case of nematics, normal stresses arise due to the departure of the director from the flow-aligned state<sup>54</sup> and can be influenced by surface anchoring.<sup>55</sup> However, the behavior of liquid crystals flowing through curved channels has not been explored. We believe that a much richer flow physics can emerge when liquid crystals flow through curved rectangular channels with homeotropic anchoring due to the interaction of conflicting director alignment imposed on the boundaries.<sup>11,40</sup> Defects may arise, but these cannot be captured with the vector-based Leslie–Ericksen theory that was used to investigate LC flows in capillary bends.<sup>23,56</sup>

In this work, we use a combination of LC microfluidic experiments and numerical methods to demonstrate novel flow control mechanisms in curvilinear microfluidic channels of varying complexity (Fig. 1A and B). The quasi-Newtonian behavior observed at low Ericksen number regime  $Er < 1$  is altered as the Ericksen number exceeds  $Er > 1$ , along with the emergence of a flow-induced director field gradient in the transverse channel direction. The transverse gradient, introduced by the channel curvature, engenders a flow-partitioning effect due to the backflow mechanism,<sup>11</sup> which is amplified by the viscous anisotropy of liquid crystals. Consequently, the throughput through the flow-aligned region scales with the degree of flow-director alignment there. Taken together, the

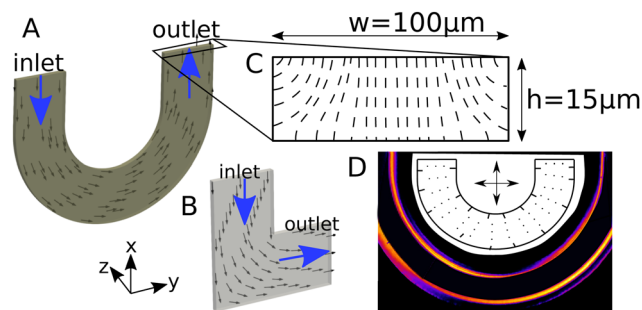


Fig. 1 Schematic description of microfluidic channels considered in this paper (A) U-channel; (B) L-channel; (C) static director field at the outlet of the U-channel; (D) light intensity under crossed polarizers and director arrangement in the center plane (inset); dots denote the director alignment perpendicular to crossed polarizers (arrows). The cross-sectional dimensions of L- and U-channels are identical. Numerical simulations assume that the inner radius of the U-bend is  $r_i = 100 \mu\text{m}$ . The coordinate system in the lower left corner refers to both U and L channels.

curvature- and Er-mediated modulation of NLC flow properties can be harnessed for potential concepts in LC-based microfluidic flow-guiding elements.

## 2. Methods and materials

### 2.1 Numerical simulations

The flow of an NLC is assumed to be solenoidal and governed by the momentum equation, which reads

$$\rho(\partial_t + u_k \partial_k) u_i = -p_{,i} + \mu u_{i,jj} + \tau_{ji}, \quad (1)$$

where  $p_{,i}$  is the pressure gradient,  $\mu$  is the Newtonian viscosity and  $\tau_{ji}$  is the viscoelastic stress<sup>57</sup>

$$\begin{aligned} \tau_{ij} = & H_{ik} Q_{kj} - Q_{ik} H_{kj} + 2\zeta(Q_{ij} + \delta_{ij}) H_{kl} Q_{kl} \zeta[(Q_{ik} + \delta_{ik}) H_{kj} \\ & + H_{ik}(Q_{kj} + \delta_{kj})] - K Q_{kl,i} Q_{kl,j}. \end{aligned} \quad (2)$$

$K$  is the elastic constant and  $Q_{ij}$  is the order parameter tensor, which evolves according to<sup>57</sup>

$$\partial_t^{\text{GS}} Q_{ij} = \Gamma H_{ij} - 2\zeta(Q_{ij} + \delta_{ij}) Q_{kl} u_{k,l}. \quad (3)$$

$\partial_t^{\text{GS}}$  represents the Gordon–Schowalter derivative, which is given by

$$\begin{aligned} \partial_t^{\text{GS}} Q_{ij} = & \frac{DQ_{ij}}{Dt} - (\zeta D_{ik} - \omega_{ik}) \cdot \left( Q_{kj} + \frac{\delta_{kj}}{3} \right) \\ & - \left( Q_{ik} + \frac{\delta_{ik}}{3} \right) \cdot (\zeta D_{kj} + \omega_{kj}). \end{aligned} \quad (4)$$

where  $\zeta$  is the slip parameter, and  $D_{ij} = \frac{u_{i,j} + u_{j,i}}{2}$ ,  $\omega_{ij} = \frac{u_{i,j} - u_{j,i}}{2}$  denote the symmetric and antisymmetric components of the velocity gradient.  $\Gamma$  in eqn (3) is the rotational diffusivity. The molecular field  $H_{ij}$  is defined in terms of the variational derivative of the Helmholtz free energy  $F$ :<sup>16</sup>

$$F = \frac{K}{2} Q_{ij,k}^2 + \frac{a}{2} Q_{ij} Q_{ij} - \frac{b}{3} Q_{ij} Q_{jk} Q_{ki} + \frac{c}{4} (Q_{ij} Q_{ij})^2, \quad (5)$$



where  $a$ ,  $b$  and  $c$  are material parameters. The relative importance of viscous and elastic effects acting on the microstructure is quantified by the Ericksen number  $Er = u_0 h / (\Gamma K)$ , where  $u_0$  is the mean flow speed and  $h = 15 \mu\text{m}$  is the channel height.

We have numerically modeled the Navier–Stokes equations coupled with the Beris–Edwards model in three dimensional U- and L-channels. Numerical solutions were obtained using the OpenFOAM solver *rheoFoamLC*.<sup>58</sup> The solver was initially based on the director framework of microstructure representation,<sup>55</sup> but its extensions allow for incorporating the  $\mathbf{Q}$ -tensor description;<sup>39</sup> the approach is capable of predicting flow-induced defects.<sup>39</sup> The system is initialized with an isotropic microstructure and static flow conditions ( $\mathbf{Q} = 0$ ,  $\mathbf{u} = 0$ ). No-slip conditions for the velocity and strong homeotropic anchoring were imposed on all walls. The fluid enters the channel with a uniform velocity at the inlet. The following material constants were used for all simulations;  $\mu = 0.2 \text{ Pa s}$ ,  $K = 40 \text{ pN}$ ,  $a = -0.2 \text{ MJ m}^{-3}$ ,  $b = 4 \text{ MJ m}^{-3}$ ,  $c = 4 \text{ MJ m}^{-3}$ ,  $\xi = 1$ ,  $\Gamma = 7.29 \text{ (Pa s)}^{-1}$ . These values are consistent with the material parameters used in similar investigations.<sup>11,59</sup> For the selected parameters and geometries, the Deborah number ( $= \frac{u_0}{\Gamma b h}$ ) is related with the Ericksen number as  $De = 4.44 \times 10^{-8}$ , which ensures that  $De \ll 1$ , and thus defect properties were weakly affected by the flow.<sup>53</sup>

## 2.2 Experimental measurements

Numerical simulations are complemented with microfluidic experiments, carried out within custom-built U- and L-shaped microchannels having rectangular cross-sections. The microchannels were assembled using polydimethylsiloxane (PDMS) molds and glass plates, bonded together after a brief plasma exposure.<sup>60</sup> The assembled channels were first treated with an aqueous solution of the silane DMOAP, that induced homeotropic surface anchoring condition on the inner walls. For the current study, we report experiments with a channel height of  $15 \mu\text{m}$  and width of  $100 \mu\text{m}$ . A single component thermotropic LC (5CB), which is nematic at room temperature, was flowed into the microchannels through cylindrical tubes embedded into holes punched through the PDMS. A precise and controlled LC flow inside the microfluidic channels was achieved by pushing a gas-tight syringe pump using a microfluidic gear pump (with a flow resolution of  $n\text{L}/\text{h}$ ). For anchoring characterization, the functionalized channels were filled with 5CB in the isotropic phase, which was first allowed to cool down to a nematic phase. No perceptible swelling of the PDMS by the 5CB was observed during the course of experiments, in agreement with the observed dependence of the swelling ratio on the substance polarity.<sup>60,61</sup> We characterize the surface- and bulk director fields using a combination of polarized optical imaging (POM), with and without the  $\lambda$ -retardation plates. The transmitted light depends on the local director alignment relative to the polarizer axes, following ref. 40 and 60.

**2.2.1 Materials.** The experiments were carried out using single component thermotropic nematic liquid crystal 4-cyano-4-pentyl-1,1-biphenyl, commonly known as 5CB. 5CB was

procured from Synthon Chemicals (Wolfen, Germany), and used without additional purification. Nematic 5CB is appropriate for the liquid crystal flow experiments due to its room temperature nematic phase, with the nematic–isotropic phase transition occurring at  $\sim 33^\circ\text{C}$ . Additionally, for the duration of the experiments presented here, 5CB is chemically stable within the polydimethylsiloxane (PDMS)-glass microfluidic devices, and has negligible swelling effect on PDMS.<sup>60</sup>

**2.2.2 Microfluidic confinement and flow setup.** The nematic 5CB was flowed through two different curvilinear geometries with rectangular cross-sections: U-shaped and L-shaped microchannels having different dimensions (height,  $h$ , and width,  $w$ ). The microfluidic channels were fabricated out of polydimethylsiloxane (PDMS, Sylgard 184, Dow Corning), a silicon-based organic polymer, on a photoresist master through a process known as soft lithography.<sup>60</sup> For the current study, we report experiments with the channel height of  $15 \mu\text{m}$ , and width of  $100 \mu\text{m}$ . The PDMS replicas were bonded to a clean microscope slide by exposing both surfaces to oxygen plasma. The microchannels were functionalized to induce a homeotropic anchoring condition (NLC anchoring perpendicular to the channel surfaces) using appropriate surface anchoring techniques. At both ends of the L-shaped microchannels, cylindrical holes with  $750 \mu\text{m}$  diameter were punched through the PDMS to provide housing for the flow tubing. Teflon tubes typically with  $300 \mu\text{m}$  inner, and  $760 \mu\text{m}$  outer diameters were inserted into each of the housings, and served as connectors for inlet-to-source and outlet-to-sink, respectively. Generation of a precise and controlled LC flow inside the microfluidic channels was achieved by a syringe pump. The channels were connected to a gas-tight microliter syringe (1001LT, Hamilton Bonaduz, Bonaduz, Switzerland), and driven by a gear pump (neMESYS, Cetoni, Korbuaen, Germany) to create a constant flow volume rate. The average flow speed through the microchannels was verified by tracking tracer particles over time (imaging focused at the channel mid-plane), and the corresponding director field was measured using polarized optical and confocal fluorescence polarized microscopy as described below. The experimental Ericksen number,  $Er = \frac{\eta v L}{K}$ , was calculated from the 5CB material properties and the measured experimental flow speed ( $\eta$  denotes the viscosity,  $v$  is the flow velocity,  $L$  is the characteristic length scale, and  $K$  is the single-elastic constant).

**2.2.3 Surface anchoring and its characterization.** For inducing homeotropic anchoring condition on the inner walls of the microchannels, the channels were first filled with a solution of Octadecyldimethyl (3-trimethoxysilyl propyl) ammonium chloride (60% in methanol, ABCR GmbH), commonly known as DMOAP, and left for 10 minutes. The channel was then rinsed with de-ionized water and heated at  $80^\circ\text{C}$  for 15 min and at  $110^\circ\text{C}$  for 1 h. After the thermal treatment, the functionalization was complete. In order to test the surface anchoring condition, the channel was filled with 5CB in isotropic phase and allowed to cool down to nematic phase. No perceptible swelling of PDMS by 5CB was observed during the course of the experiments, in agreement with the observed dependence





of the swelling ratio on the substance polarity.<sup>60,61</sup> The surface anchoring is characterized by studying the director field in the bulk and close to the channel walls using polarized optical imaging (POM) as described in the next section.

**2.2.4 Polarized optical imaging (POM).** The NLC director alignment within the PDMS-glass microfluidic channels was studied using a polarized light microscope (Eclipse LV100N-POL, Nikon), equipped with different objectives  $\times 5$ ,  $\times 10$ ,  $\times 20$ , and  $\times 40$  objectives. The sample was maintained at room temperature. Various experimental cases were captured using the following orientations of the crossed-polarizers using transmitted white light: (a) the microfluidic channel arm parallel to one of the crossed-polarizers, (b) the channels oriented at  $45^\circ$  with respect to the polarizers, and (c) with and without the insertion of a 530 nm phase-retardation plate. POM images were acquired using a digital Canon EOS77D camera. The acquired POM data were quantified using a combination of ImageJ and MATLAB softwares, to finally extract the intensity plots (Fig. 5 in appendix B) due to the flow-induced director fields.<sup>10,11</sup>

### 3. Results

#### 3.1 Analytical prediction

Assuming that the liquid crystal is uniaxial and the order parameter is constant, the Beris–Edwards model (with  $\zeta = 1$ ) can be simplified to the Leslie–Ericksen theory and the steady-state angular momentum balance equation reduces to a non-linear Poisson equation

$$(\partial_{yy} + \partial_{zz})\theta + u_{x,z}Er \sin^2 \theta = 0, \quad (6)$$

where  $\theta$  is the angle between the director and the flow direction (eqn (6) is derived in Appendix A). When  $Er \ll 1$ , wall imposed homeotropic anchoring forces the director to align in the  $y$ - $z$  plane, normal to the flow direction. When  $Er = O(1)$  viscous effects become significant, manifesting through the rotation of the director field towards the Leslie angle, which is aligned with the flow direction in the limit of uniaxial ordering with  $\zeta = 1$ . Eqn (6) suggests that the local velocity gradient amplifies the effect of Ericksen number: flow alignment is promoted in regions of elevated shear rate.

#### 3.2 U-bend

The analytical result has been qualitatively confirmed by experimental measurements and numerical calculations. The director aligns in the  $z$ -direction at  $Er \ll 1$ , as indicated by the uniform dark signal throughout the U-bend (Fig. 1D). At  $Er = O(1)$  the director alignment is also affected by viscous effects. In creeping flows, the peak velocity is displaced towards the bend axis<sup>54,55</sup> and the resulting elevated shear rate is responsible for the emergence of the flow-aligned director field at the inside of the bend at  $Er = 4$ . The result is experimentally observed through a non-zero light intensity signal near the inner wall (upper row in Fig. 2A), and is qualitatively confirmed by numerical simulations (Fig. 2B and C). The size of the flow-aligned region scales with the Ericksen number. For  $Er = 6$ , the elasticity dominated region of the director field is confined to the outer bend wall (middle row in Fig. 2), where there is consequently relatively little flow. Further evidence for the shear-induced propagation of the flow-aligned region towards the outside of the bend is provided in Fig. 5.

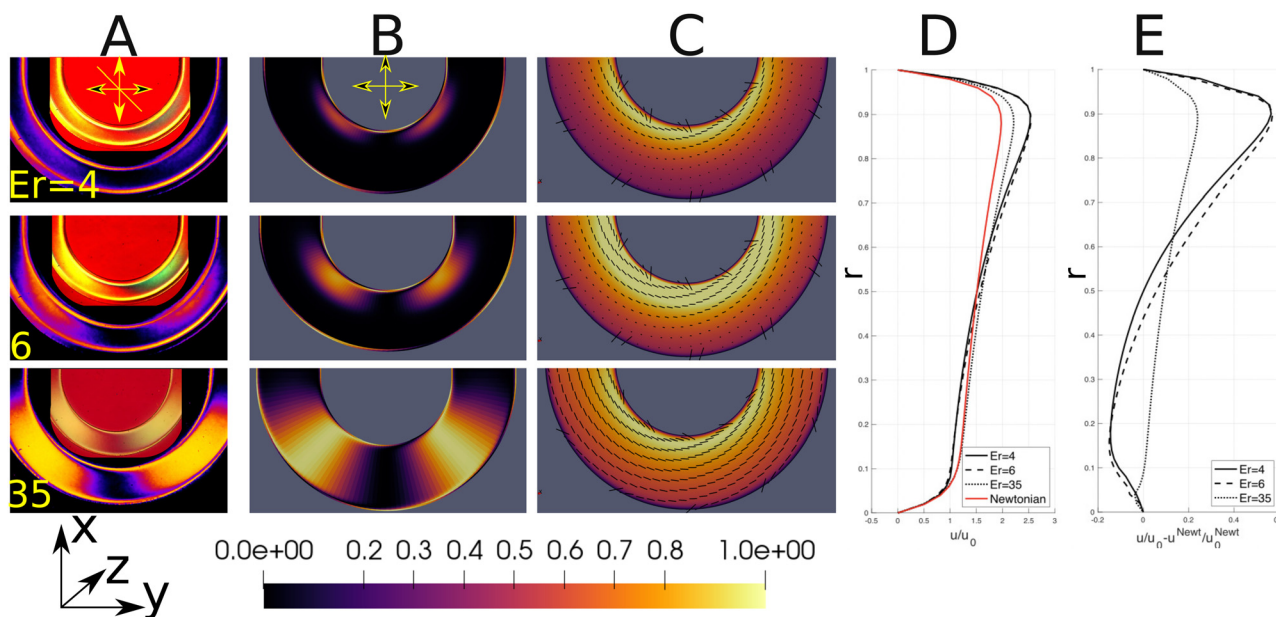


**Fig. 2** Director alignment in a flow through U-bend. (A) Experimental micrographs showing transmitted light intensity under crossed polarizers. Inset: polarized micrograph with a  $\lambda$ -retardation plate; the yellow and the blue-green signals respectively denote director alignment parallel and perpendicular to the retardation plate. (B) Numerical prediction of intensity under crossed polarizers (calculated as  $4n_x^2 n_y^2$ ) in the symmetry plane. (C) Density plots of velocity magnitude scaled by the maximum flow speed and glyphs of the director field (symmetry plane). (D) Velocity profile in the center of the bend. (E) Amplification of flow asymmetry induced by the anisotropic microstructure.  $r$  denotes the normalized distance from the outer to the inner bend wall,  $u$  is the flow speed in the centerplane, superscript  $N$  and subscript  $0$  refer to the Newtonian fluid and the mean flow speed, respectively.



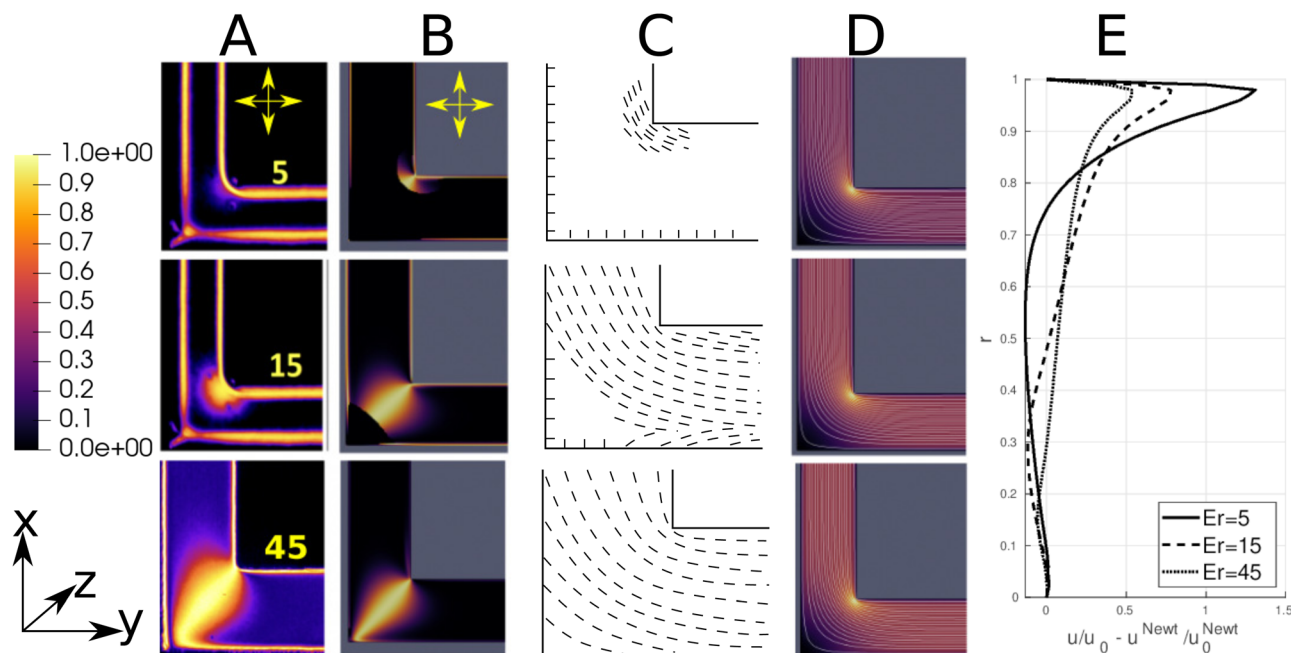


Fig. 3 Director alignment in a flow through the L-channel. (A) Intensity image obtained with crossed polarizers. (B) Numerical prediction of intensity with crossed polarizers (calculated as  $4n_x^2 n_y^2$ ). (C) Glyphs of the director field. (D) Contours of flow magnitude scaled by the maximum flow speed. The Ericksen number is denoted by the white number in the lower left corner of column A pictures. (E) Effect of nematic liquid crystals on the amplification of flow asymmetry (in the symmetry of the U-bend) with respect to a Newtonian fluid.  $r$  denotes the normalized distance from the outer to the inner corner,  $u$  is the flow speed in the centerplane, superscript  $N$  and subscript  $0$  refer to the Newtonian fluid and the mean flow speed, respectively.

The combination of nematic viscoelasticity and geometric curvature produces variable director alignment across the channel. More flow is promoted in regions where flow alignment is achieved. Fig. 2D and E show that the presence of nematic liquid crystals amplifies the uneven flow distribution introduced by the geometry. Novel mechanisms for flow partitioning controlled by the Ericksen number may thus be identified. The potential for flow tuning is weaker at high Ericksen numbers, where the dominance of viscous effects results in complete flow alignment (lower row in Fig. 2) and thus nearly uniform effective viscosity. The corresponding velocity profile (dotted line in Fig. 2D) is much more similar to the Newtonian result than at intermediate Er. Additional simulations (not reported here) show that as the Ericksen number increases, viscous effects dominate the director alignment and stress distribution, resulting in the Newtonian velocity profile ( $u/u_0 - u^N/u_0^N = 0$ ).<sup>11</sup>

### 3.3 L-channel

The physics governing microstructure arrangement in an L-channel is qualitatively similar to the U-bend. Here, the change in flow direction occurs over a smaller length scale, so flow-aligning effects are more localized near the inner corner. The effect can be seen experimentally in Fig. 3A and numerically in Fig. 3B and C. Both experiments and simulations show that higher flow speeds in the L-channel occur near the inner corner. The crossed polarizer images indicate that director alignment is initiated there. Similar to the U-bend flow, the curvature in the L-channel introduces a positive feedback mechanism: reduced effective viscosity in the flow-aligned

inner corner promotes further flow there (indicated by tighter streamline concentrations in Fig. 3D). At  $Er = 15$ , the director remains unaligned with the flow only in the outer corner of the elbow, which results in a stagnation region there. The L-bend is thus seen to act like a microfluidic valve, where the effective valve throat is controlled by the Ericksen number. The valve effect becomes stronger as the radius of curvature decreases; at the inner corner of the L-bend the relative increase in velocity is up to three times larger than near the inner wall of the U-bend (Fig. 3E). The effect of flow asymmetry is reduced at high Er, where flow dynamics dominate director alignment and the overall rheology tends toward a Newtonian fluid (Fig. 3E).

#### 3.3.1 Flow tuning through defect-promoted shear banding.

Numerical simulations show that the separation between the flow- and z-aligned director field induces defects (dark dot on the right side of Fig. 4a) in the microstructure. Increasing Er moves the defect towards the outer wall, which manifests through the displacement of the director transition region (Fig. 4b) and the accompanying lower order parameter region (Fig. 4c). The presence of a defect affects the velocity gradient (Fig. 4d) and produces a novel type of shear banding. The location of the defect marks the onset of the flow-aligned director field and thus the defect separates lower shear rate and higher shear rate regions. This provides a novel type of flow transition; previous studies of shear banding in liquid crystals are driven by the nematic–isotropic transition arising from flow<sup>62</sup> or temperature<sup>11</sup> effects.

Flow control across a range of Ericksen numbers can be achieved by managing the size of the stagnation region. Fig. 4e



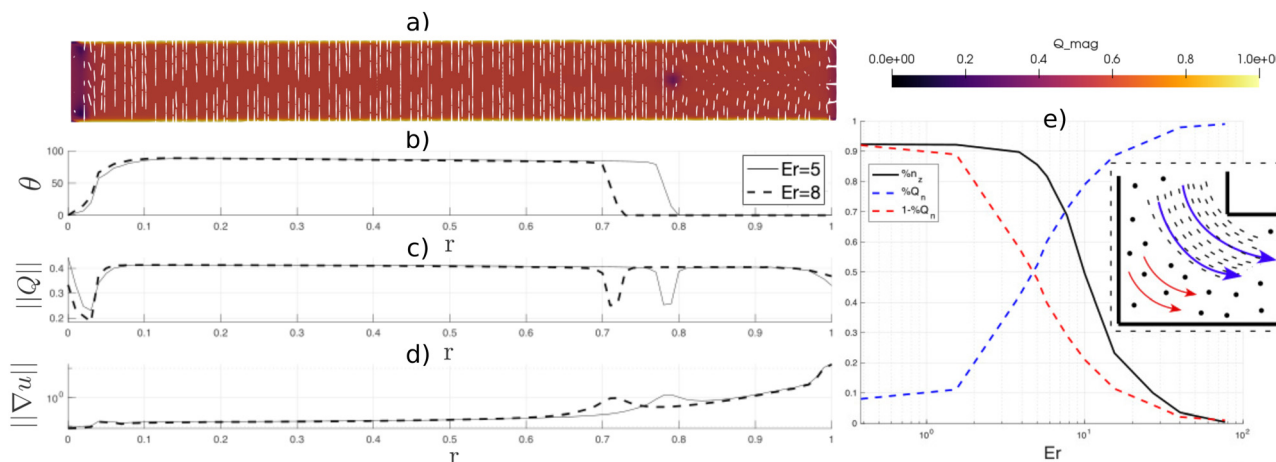


**Fig. 4** (a) Order parameter and director field (white rods) between the outer and inner corner at  $Er = 5$ ; (b) variation of the director angle between L-bend corners; (c) variation of the order parameter between L-bend corners; (d) velocity gradient between L-bend corners; (e) channeling NLC flows through curved channels over a range of Ericksen numbers.  $\%n_z$  is the fraction of the corner region occupied by the z-aligned director field, and  $\%Q_n$  represents the flow fraction (blue arrows in the inset) through the region where the  $\mathbf{n}$  (black dashed lines in the inset) aligns with the flow. Red arrows in the inset represent the velocity vectors in the region where  $\mathbf{n}$  aligns in the flow transverse direction (denoted by black dots).

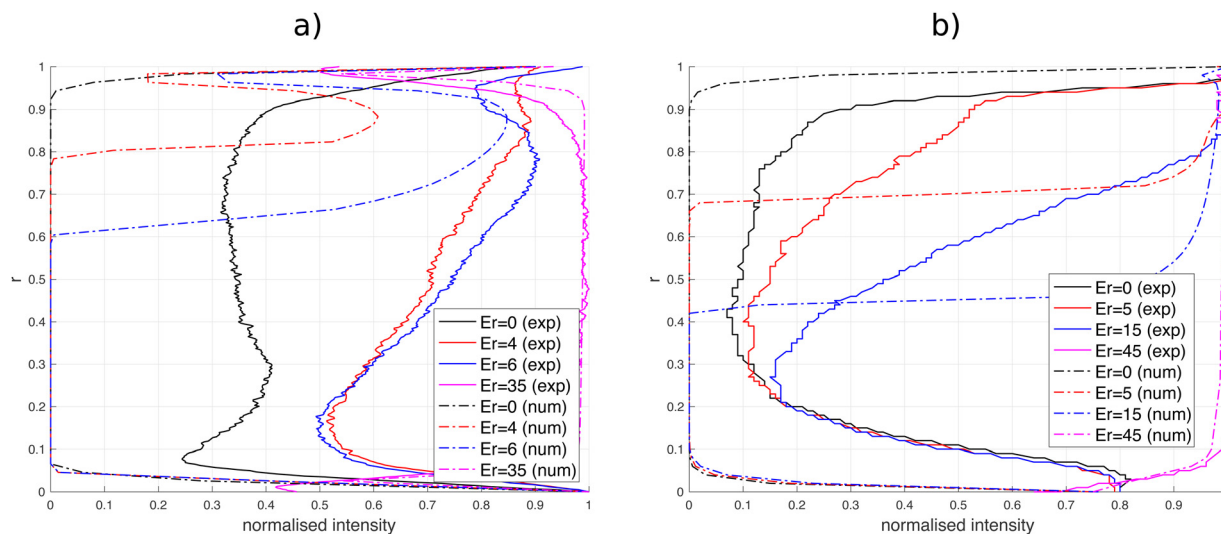


**Fig. 5** Normalized light intensity (a) at a  $135^\circ$  angle from the U-bend entrance; (b) between the inner and outer corner of the L-bend.  $r$  denotes the normalized distance from the outer U-bend wall and from then inner corner in the L-bend, respectively.

shows that as the size of the flow-transverse director region decreases (solid black line), the throughput through the flow-aligned region local to the inner corner increases (blue dashed line). Thus, flow channelization is induced by the anisotropic director field, and the throughput near the inner corner ( $r > 0.9$ ) can be up to 50% larger for nematic flows than for Newtonian fluids under identical channel curvature conditions.

## 4. Conclusions

Nematic liquid crystals flowing through curvilinear microchannels produce a transverse gradient of the director field, which can feedback into the flow field and produce curvature-director-flow

coupling. For ranges of Ericksen number, this coupling can create abrupt flow changes, thereby inducing topological defects and generating binary flow states. Flow alignment of the director field initiates at  $Er \approx 2$  and is promoted (hindered) in locations of higher (lower) flow speeds. The effect becomes stronger as the geometric curvature increases, and produces a positive feedback effect: as the director alignment increases, the apparent viscosity reduces, along with the reduction of boundary layer size. This has a channeling effect on the velocity distribution, and more flow is promoted in the flow-aligned region. Decreasing geometry curvature increases the degree of flow asymmetry; consequently, higher Ericksen numbers are required to promote the complete flow alignment. These findings could guide the development of potential applications, for



instance, featureless flow-guidance circuits, LC-based microfluidic logic gates and optofluidic switches.

Liquid crystals offer a promising avenue for advancing microfluidic flow control devices. However, their applicability is subject to potential limitations. Scaling problems may arise in larger geometries, where  $Er \gg 1$  produces Newtonian behavior, as discussed in Section 3.2. Additionally, liquid crystals are prone to forming defect structures, the occurrence of which requires careful handling of the microfluidic device. Finally, the utility of microfluidic devices is constrained by the temperature sensitivity of liquid crystals because anisotropic properties are lost below the nematic–isotropic transition temperature. Curvilinear microfluidic experiments with lyotropic chromonic phases could offer tangible avenues to offset the temperature sensitivity of thermotropic phases, specifically by tuning the concentration of the lyotropic chromonic surfactants.<sup>63,64</sup> Owing to the role of chromonic phases in diverse applications, studies on their flow through curvilinear geometries could be relevant for manipulation of different drugs, dye molecules and nucleic acids.

In future work, we aim to investigate microfluidic geometries where extensional flow plays a role in the liquid crystal alignment; examples include expansions, T and Y junctions. Additional investigations are also underway to assess the potential of using electric fields in flow manipulation.

## Data availability

All data are available from the corresponding author on reasonable request.

## Author contributions

R. P. and K. F. conducted numerical simulations, A. S. carried out experiments. All authors contributed equally to formal analysis and writing.

## Conflicts of interest

There are no conflicts to declare.

## Appendices

### A Analytical quantification of the flow effect on the director field

The angular momentum balance of the Beris–Edwards model in the uniaxial, constant order parameter limit reduces to the Leslie–Ericksen theory.<sup>33,56,65</sup>

$$\gamma_1(n_{i,t} + u_j n_{i,j}) = h_i - n_i n_j h_j - \gamma_2 [D_{ij} n_j - (n_i n_j n_k D_{jk})] - \gamma_1 n_j \omega_{ji}, \quad (7)$$

where  $h_i = K n_{i,jj}$  is the molecular field. The coefficients  $\gamma_1$  and  $\gamma_2$  can be expressed in terms of the Beris–Edwards material

parameters<sup>19</sup>

$$\gamma_1 = \frac{2Q^2}{\Gamma}, \quad \gamma_2 = -\frac{2(2+Q)\xi}{3\Gamma}. \quad (8)$$

Introducing the dimensionless parameters

$$\tilde{u}_i = \frac{u_i}{u_0}, \quad \tilde{\partial}_x = \frac{1}{h} \partial_x, \quad \tilde{t} = \frac{h}{u_0} t, \quad \tilde{x}_i = \frac{x_i}{h}, \quad \tilde{h}_i = \frac{K}{h^2} h_i, \quad (9)$$

the director evolution equation can be written as

$$n_{i,t} + \tilde{u}_j n_{i,j} = Er^{-1} (\tilde{h}_i - n_i n_j \tilde{h}_j) - \frac{\gamma_2}{\gamma_1} [\tilde{D}_{ij} n_j - (n_i n_j n_k \tilde{D}_{jk})] - n_j \tilde{\omega}_{ji}, \quad (10)$$

where  $Er = \frac{2u_0 h}{K\Gamma}$ . The general problem may be simplified by making the following assumptions:

- The system is in the steady state.
- The system is fully developed.
- The order parameter is constant  $Q = 1$ .
- We have chosen  $\xi = 1$ , so from eqn (8) we have  $\frac{\gamma_2}{\gamma_1} = -1$ .

With the assumptions above, the angular momentum eqn (10) reduces to

$$n_{i,jj} - \underline{n_i n_j n_{j,kk}} - \left( n_j \tilde{u}_{i,j} - \underline{n_i n_j n_k \tilde{u}_{j,k}} \right) Er = 0, \quad (11)$$

where the underlined terms ensure that the director retains unit magnitude. The x-component of the director balance equation reads

$$n_{x,\tilde{y}y} + n_{x,\tilde{z}z} - [n_y \tilde{u}_{x,\tilde{y}} + n_z \tilde{u}_{x,\tilde{z}}](1 - n_x^2) Er - n_x [n_x (n_{x,\tilde{y}y} + n_{x,\tilde{z}z}) + n_y (n_{y,\tilde{y}y} + n_{y,\tilde{z}z}) + n_z (n_{z,\tilde{y}y} + n_{z,\tilde{z}z})] = 0. \quad (12)$$

Assuming that the director remains in the x–z plane (with the flow taking place in the x-direction and the velocity gradient in the z-direction), we can express its components in terms of the polar angle  $\theta$  that it makes with the flow direction ( $\mathbf{n} = [n_x, n_y, n_z] = [\cos \theta, 0, \sin \theta]$ ), and the director balance simplifies to

$$(\partial_{\tilde{y}y} + \partial_{\tilde{z}z})\theta + \tilde{u}_{\tilde{x},\tilde{z}} Er \sin^2 \theta = 0. \quad (13)$$

### B. Light intensity in the U- and L-channels

Fig. 5 compares the experimental and numerical intensity profiles across the U- and L-bends. Experimental measurements are z-integrated over the channel depth, while the intensity in numerical simulations is taken at the centerplane. Both approaches indicate a higher light intensity at the inner inner wall/corner ( $r > 0.5$ ) in the U-bend/L-channel that is caused by the improved flow/director alignment there (Fig. 5a and b). The sharp transition predicted by the numerical simulations is a manifestation of the defect boundary, as discussed in Section 3.3.1.

## Acknowledgements

KF and RP acknowledge the EPSRC project the Centre in Advanced Fluid Engineering for Digital Manufacturing (grant





no. EP/R00482X/1) and Unilever plc for financial support. KF and RP would like to acknowledge the assistance given by Research IT and the use of the Computational Shared Facility at The University of Manchester. AS thanks the Luxembourg National Research Fund's ATTRACT Investigator Grant (grant no. A17/MS/11572821/MBRACE) and CORE Grant (C19/MS/13719464/TOPOFLUME/Sengupta) for supporting this work.

## Notes and references

- H. Bruus, *Theoretical Microfluidics*, Oxford University Press, Oxford (UK), 2008.
- G. M. Whitesides, *Nature*, 2006, **442**, 368–373.
- T. Pfohl, F. Mugele, R. Seemann and S. Herminghaus, *Chem. Phys. Chem.*, 2003, **4**, 1291–1298.
- G. Kunti, J. Dhar, A. Bhattacharya and S. Chakraborty, *Phys. Fluids*, 2019, **9**, 092003.
- F. Paratore, V. Bacheva, M. Bercovici and G. V. Kaigala, *Nat. Rev. Chem.*, 2021, **6**, 70–80.
- O. J. Dressler, R. M. Maceiczky, S.-I. Chang and A. J. deMello, *SLAS Discovery*, 2014, **19**, 483–496.
- K. W. Oh, *Micromachines*, 2020, **11**, 370.
- D. J. Beebe, G. A. Mensing and G. M. Walker, *Annu. Rev. Biomed. Eng.*, 2002, **4**, 261–286.
- J. Priyadarshani, T. Roy, S. Das and S. Chakraborty, *ACS Biomater. Sci. Eng.*, 2021, **7**, 483–496.
- A. Sengupta, S. Herminghaus and C. Bahr, *Liq. Cryst. Rev.*, 2014, **2**, 73–110.
- A. Sengupta, U. Tkalec, M. Ravnik, J. M. Yeomans, C. Bahr and S. Herminghaus, *Phys. Rev. Lett.*, 2013, **110**, 048303.
- A. Sengupta, C. Bahr and S. Herminghaus, *Soft Matter*, 2013, **9**, 7251–7260.
- M. Ravnik and J. M. Yeomans, *Phys. Rev. Lett.*, 2013, **110**, 026001.
- Z. Kos and M. Ravnik, *Sci. Rep.*, 2020, **10**, 1446.
- I. Stewart, *The Static and Dynamic Continuum Theory of Liquid Crystals: A Mathematical Introduction*, Taylor and Francis, London, 2004.
- P. de Gennes and J. Prost, *The Physics of Liquid Crystals*, Oxford Science Publications, 1993.
- Y. Xu, A. M. Rather, Y. Yao, J.-C. Fang, R. S. Mamtani, R. K. A. Bennett, R. G. Atta, S. Adera, U. Tkalec and X. Wang, *Sci. Adv.*, 2021, **7**, eabi7607.
- Z. Khoshbin, K. Abnous, S. M. Taghdisi and A. Verdian, *Trends Anal. Chem.*, 2021, **142**, 116325.
- S. J. Woltman, G. D. Jay and G. P. Crawford, *Nat. Mater.*, 2007, **6**, 116325.
- K. Fedorowicz and R. Prosser, *Liq. Cryst.*, 2023, 1–24.
- P. Pieranski and E. Guyon, *Phys. Lett. A*, 1974, **49**, 237–238.
- A. Sengupta, *Int. J. Mol. Sci.*, 2013, **14**, 22826–22844.
- P. Steffen, E. Stellamanns and A. Sengupta, *Phys. Fluids*, 2021, **33**, 072005.
- Y.-J. Na, T.-Y. Yoon, S. Park, B. Lee and S.-D. Lee, *Chem. Phys. Chem.*, 2010, **11**, 101–104.
- D. Wee, S. H. Hwang, Y. S. Song and J. R. Youn, *Soft Matter*, 2016, **12**, 3868–3876.
- J. G. Cuennet, A. E. Vasdekis and D. Psaltis, *Lab Chip*, 2013, **13**, 2721–2726.
- A. Sengupta, S. Herminghaus and C. Bahr, *Appl. Phys. Lett.*, 2012, **101**, 164101.
- J.-C. Eichler, R. A. Skutnik, A. Sengupta, M. G. Mazza and M. Schoen, *Mol. Phys.*, 2019, **117**, 3715–3733.
- Y. Liu, D. Cheng, I.-H. Lin, N. L. Abbott and H. Jiang, *Lab Chip*, 2012, **12**, 3746–3753.
- D. Vettese, *Nat. Photonics*, 2010, **4**, 752–754.
- J. G. Cuennet, A. E. Vasdekis, L. De Sio and D. Psaltis, *Nat. Photonics*, 2011, **5**, 234–238.
- S. Čopar, Z. Kos, T. Emeršič and U. Tkalec, *Nat. Commun.*, 2020, **11**, 59.
- C. Denniston, E. Orlandini and J. M. Yeomans, *Phys. Rev. E*, 2001, **63**, 056702.
- C. Denniston, E. Orlandini and J. Yeomans, *Comput. Theor. Polym. Sci.*, 2001, **11**, 389–395.
- M. Kleman and O. D. Lavrentovich, *Soft Matter Physics: An Introduction*, Springer New York, 2003.
- J. Quintans-Carou, B. R. Duffy, N. J. Mottram and S. K. Wilson, *Phys. Fluids*, 2006, **18**, 027105.
- P. A. Cruz, M. F. Tome, I. W. Stewart and S. McKee, *J. Comput. Phys.*, 2013, **247**, 109–136.
- A. D. Rey and M. M. Denn, *Annu. Rev. Fluid Mech.*, 2002, **34**, 233–266.
- K. Fedorowicz and R. Prosser, *J. Non-Newton. Fluid Mech.*, 2022, **310**, 104949.
- A. Sengupta, *Topological microfluidics - nematic liquid crystals and nematic colloids in microfluidic environment*, Springer, 2013.
- S. Mondal, I. M. Griffiths, F. Charlet and A. Majumdar, *Fluids*, 2018, **3**, 39.
- M. Srinivasarao, *Spontaneous Emergence of Chirality*, John Wiley & Sons, Ltd, 2021, ch. 5, pp. 311–346.
- K. Nayani, R. Chang, J. Fu, P. W. Ellis, A. Fernandez-Nieves, J. O. Park and M. Srinivasarao, *Nat. Commun.*, 2015, **6**, 8067.
- J. Fu, K. Nayani, J. O. Park and M. Srinivasarao, *NPG Asia Mater.*, 2017, **9**, e393.
- C. M. Tone, A. Zizzari, L. Spina, M. Bianco, M. P. De Santo, V. Arima, R. C. Barberi and F. Ciuchi, *Langmuir*, 2023, **39**, 6134–6141.
- W. R. Dean, *Proc. R. Soc. Lond. A*, 1928, 121402–121420.
- D. Di Carlo, *Lab Chip*, 2009, **9**, 3038–3046.
- V. Steinberg, *Annu. Rev. Fluid Mech.*, 2021, **53**, 27–58.
- Y. Fan, R. I. Tanner and N. Phan-Thien, *J. Fluid Mech.*, 2001, **440**, 327–357.
- A. Robertson and S. Muller, *Int. J. Non-Linear Mech.*, 1996, **31**, 1–20.
- A. Sengupta, C. Pieper, J. Enderlein, C. Bahr and S. Herminghaus, *Soft Matter*, 2013, **9**, 1937–1946.
- L. Giomi, Z. Kos, M. Ravnik and A. Sengupta, *Proc. Natl. Acad. Sci. U. S. A.*, 2017, **114**, E5771–E5777.
- Z. Kos, M. Ravnik and S. Zumer, *Liq. Cryst.*, 2017, **44**, 2161–2171.



- 54 K. Fedorowicz and R. Prosser, *J. Non-Newton. Fluid Mech.*, 2022, **300**, 104716.
- 55 K. Fedorowicz and R. Prosser, *Phys. Fluids*, 2022, **34**, 063106.
- 56 F. M. Leslie, *Q. J. Mech. Appl. Math.*, 1966, **19**, 357–370.
- 57 A. Beris and B. Edwards, *Thermodynamics of Flowing Systems with an Internal Microstructure*, Oxford University Press, 1994.
- 58 K. Fedorowicz, Source code of the rheoFoamLC solver and the implementation of constitutive equations, 2022, <https://github.com/KamilFedorowicz>.
- 59 M. Ravnik and S. Zumer, *Liq. Cryst.*, 2009, **36**, 1201–1214.
- 60 A. Sengupta, B. Schulz, E. Ouskova and C. Bahr, *Microfluid. Nanofluid.*, 2012, **13**, 941–955.
- 61 A. Sengupta, *Liq. Cryst.*, 2014, **41**, 290–301.
- 62 J. K. G. Dhont, M. P. Lettinga, Z. Dogic, T. A. J. Lenstra, H. Wang, S. Rathgeber, P. Carletto, L. Willner, H. Frielinghaus and P. Lindner, *Faraday Discuss.*, 2003, **123**, 157–172.
- 63 A. Sharma, I. L. H. Ong and A. Sengupta, *Crystals*, 2021, **11**, 35.
- 64 V. Ulaganathan and A. Sengupta, *J. Colloid Interface Sci.*, 2023, **649**, 302–312.
- 65 O. Parodi, *J. Phys.*, 1970, **31**, 581–584.

